Table S1. Summary statistics of the total of 10 observed dust storms with significant at 5% (larger than one page, upload as a separate file).

Table S2. Statistical summary of the multiple regression model.

Coefficients	Estimate	Std. Error	t-value	Pr(>|t|)
b_0	2.69558	0.64111	4.205	4.45E-5 ***
b_1	-0.27191	0.05175	-5.254	4.94E-7 ***
b_2	-0.06982	0.0289	-2.416	0.01688 *
b_3	0.00893	0.00115	7.748	1.23E-12 ***
b_4	6.095E-4	3.574E-4	1.705	0.09023 ·
b_5	0.00247	8.675E-4	2.845	0.00505 **

Residual standard error: 0.437 on 152 degrees of freedom; Multiple R-squared: 0.7074, Adjusted R-squared: 0.6977; F-statistic: 73.48 on 5 and 152 DF, p-value: < 2.2e-16.

Movie S1. The severe dust storms occurring on 17 April 2017.

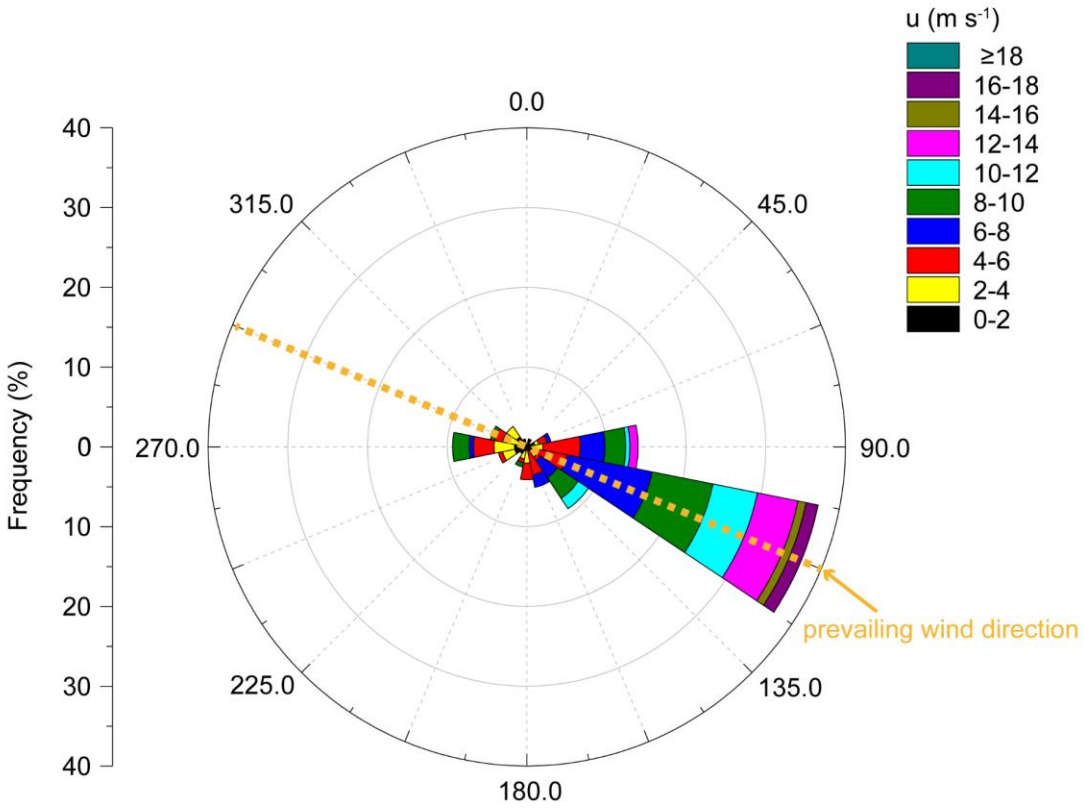

Fig. S1. Wind rose of the QLOA during the observational period. The QLOA has a prevailing wind direction with a mean angle of ~247.5° with respect to the North (about a frequency of 74.6%).

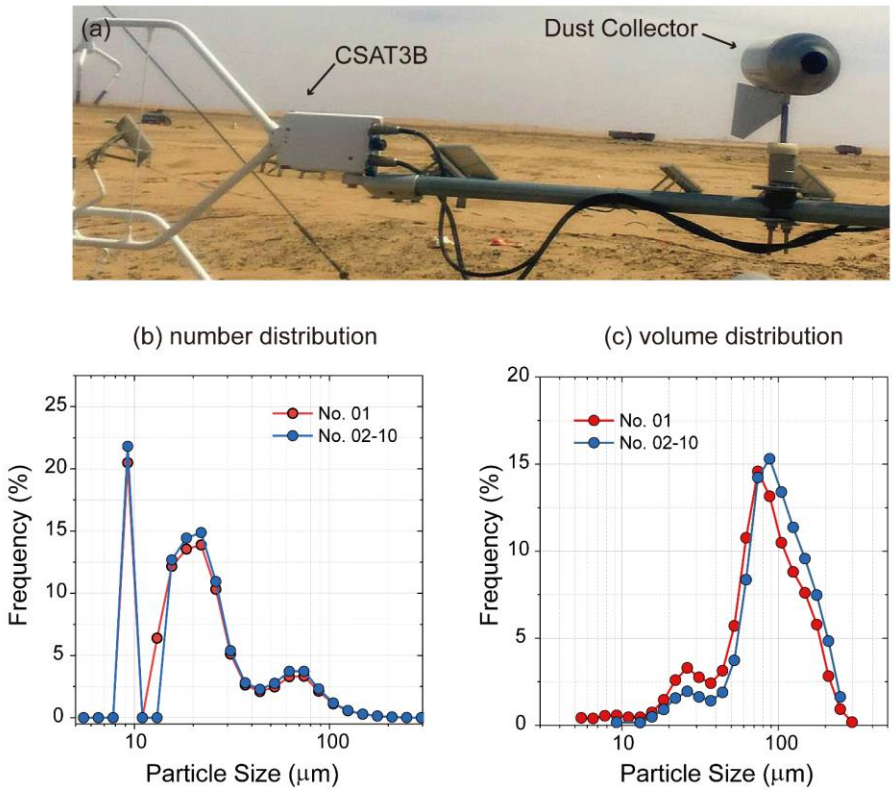

Fig. S2. Size distributions of the airborne dust particles collected at the S9 site (5 m above the ground). (a) A dust collector was mounted on a horizontally orientated steel bar. (b) Number distribution of the collected airborne dust particles during No. 01 and No. 02-10 dust storms. (c) The corresponding volume distribution of the collected airborne dust particles. Particle size analysis was performed using the Microtrac S3500 tri-laser particle size analyzer. Since the collected airborne dust particles of single dust storms are very few (i.e. No. 02-10 events), it is difficult to measure the size distribution of single dust storms by the collected dust sample. Consequently, the collected dust particles from No. 02-10 dust storms were combined to obtain a mean size distribution, as shown in Figs. S2a and S2b.

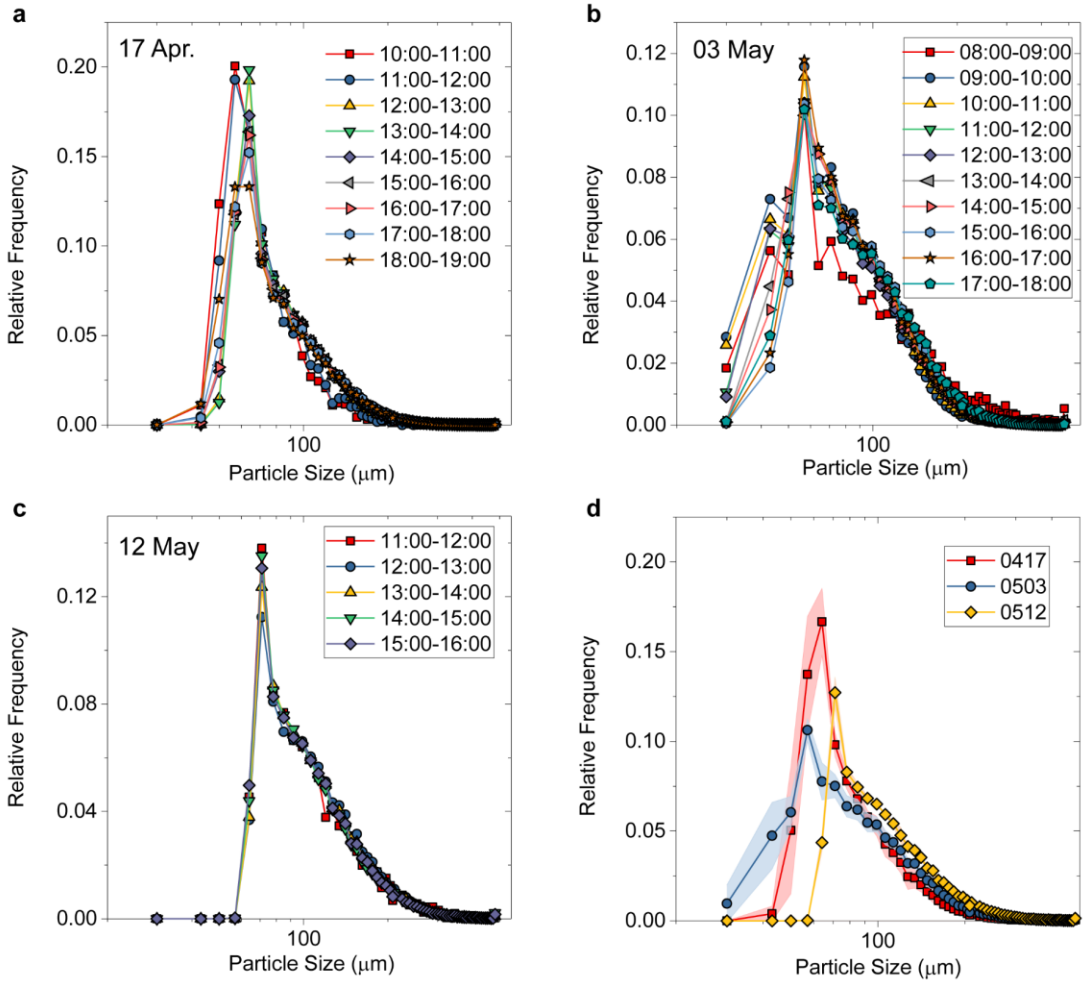

Fig. S3. Examples of the particle size distribution (PSD) of saltating particles at 0.2 m above the ground. (a)-(c) The mean PSD of dust particles at different periods. (d) Comparison of the PSD of sand particles in the different dust storms. Symbols denote the mean values, and the light shadows denote the standard deviations.

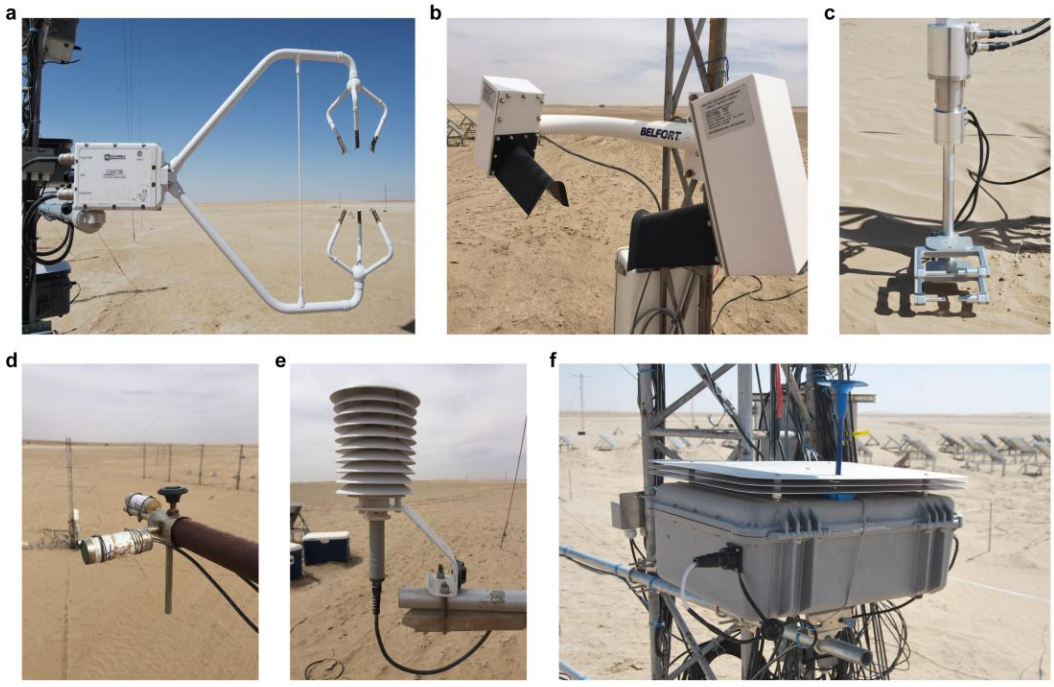

Fig. S4. Photos of the instruments used in our observations. (a) CSAT3B, (b) Belfort Model 6000, (c) SPC-91, (d) VREFM, (e) Young Model 41003, and (f) DustTrak II Model 8530EP.

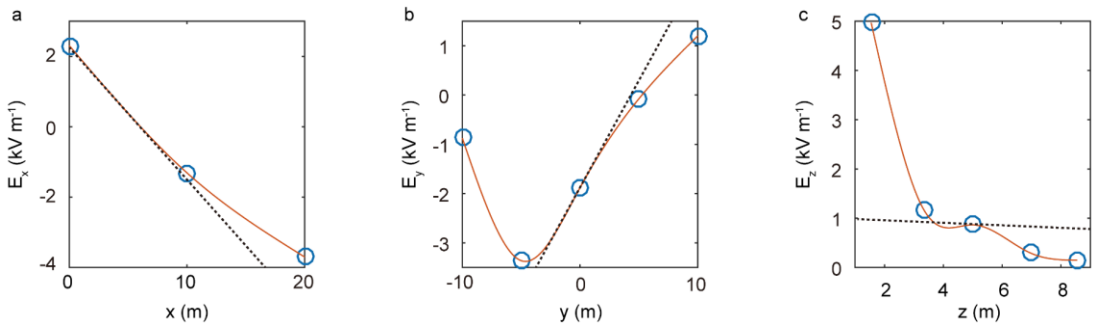

Fig. S5. Example of the calculating the divergence of the electric field. (a)-(c) The natural cubic spline of the measured electric fields in the three mutually perpendicular monitoring networks. Circles represent the measured electric fields, solid lines represent the natural cubic spline, and the dashed lines represent the tangent at S9 of which slopes are the derivatives $\partial \mathrm{E}_i / \partial x_i$. The calculation of the divergence of the electric fields is based on the natural cubic spline interpolating the measured electric field intensities. For such natural cubic spline approximating differentiation, the error is $\|s'-y'\| \le h/\pi \|y''\|$, where s is the interpolating spline; $h = \max\{h_i\}$ is the maximum interval (*Hanke, M., and Scherzer, O., 2001. Inverse problems light: numerical differentiation. The American Mathematical Monthly, 108(6), 512-521*). In this study, $\|s'-y'\| \le 3.18\|y''\|$ is very small compared to s' that is on the order of 10^3-10^4 V m^{-1} during dust storms.

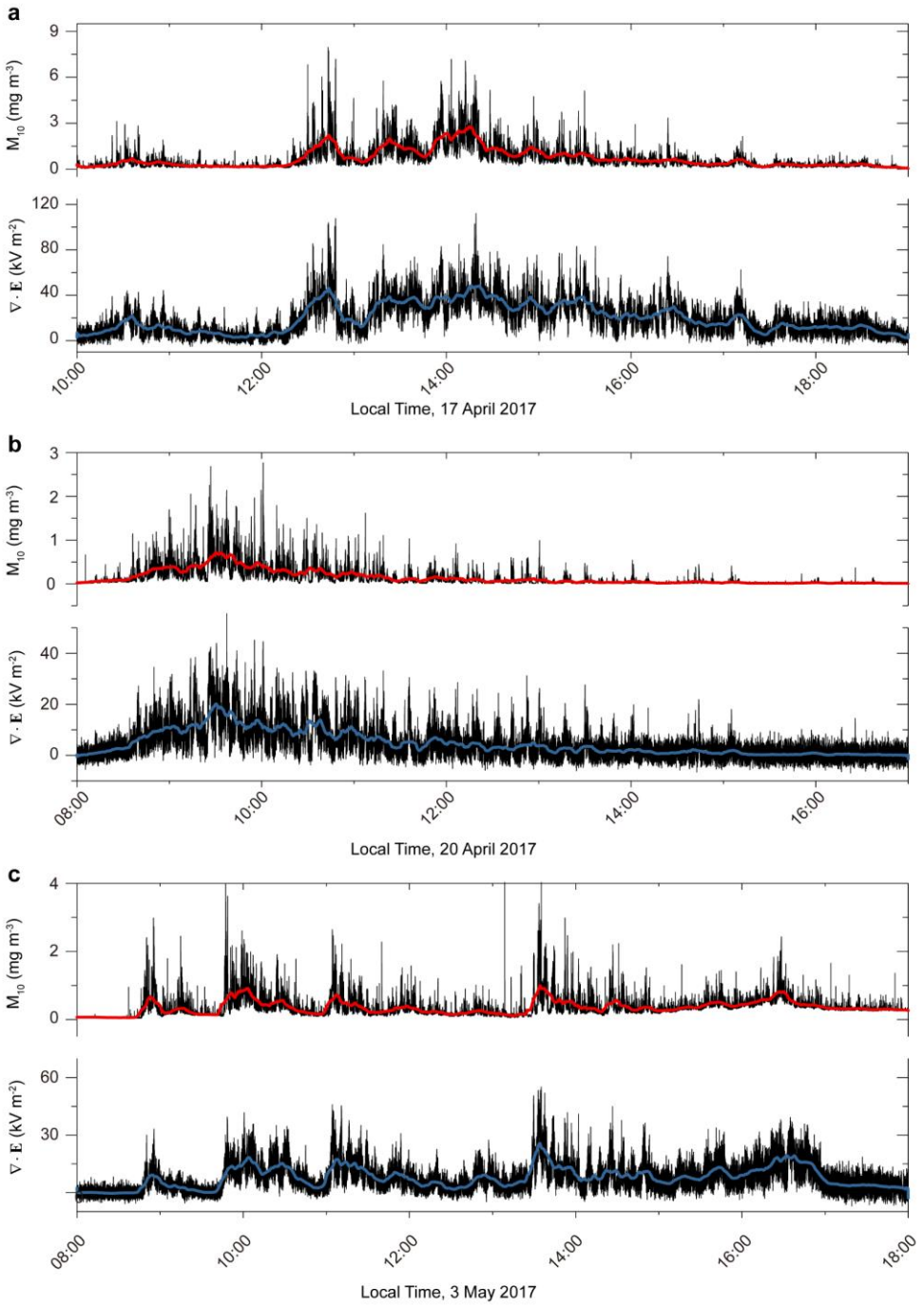

Fig. S6. Examples of the 10-minute moving averages of the divergence of the electric field and dust concentration. (a)-(c) The black lines represent the original data; and the color lines represent the moving averages. The central moving average, using data equally spaced on either side of the point in the series, is used to compute the 10 min average time series. Actually, the span of moving average is 601 data points (10 min and 1 s) because the central moving average requires an odd number of data points in the sample window.

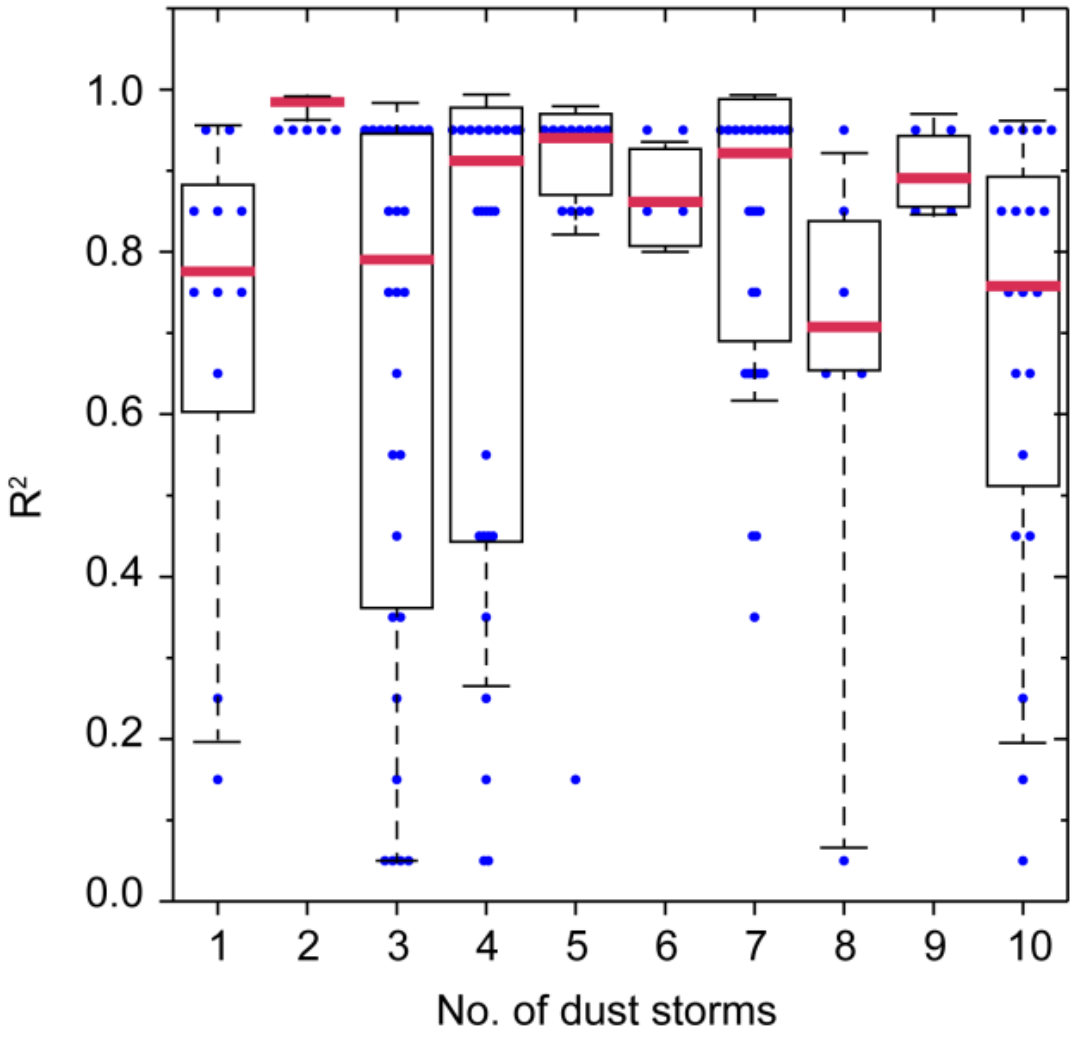

Fig. S7. Box plots of R^2 of SLR of for all the 10 dust storms. The central red marks show the medians, and the edges of the box show the first and third quartiles.

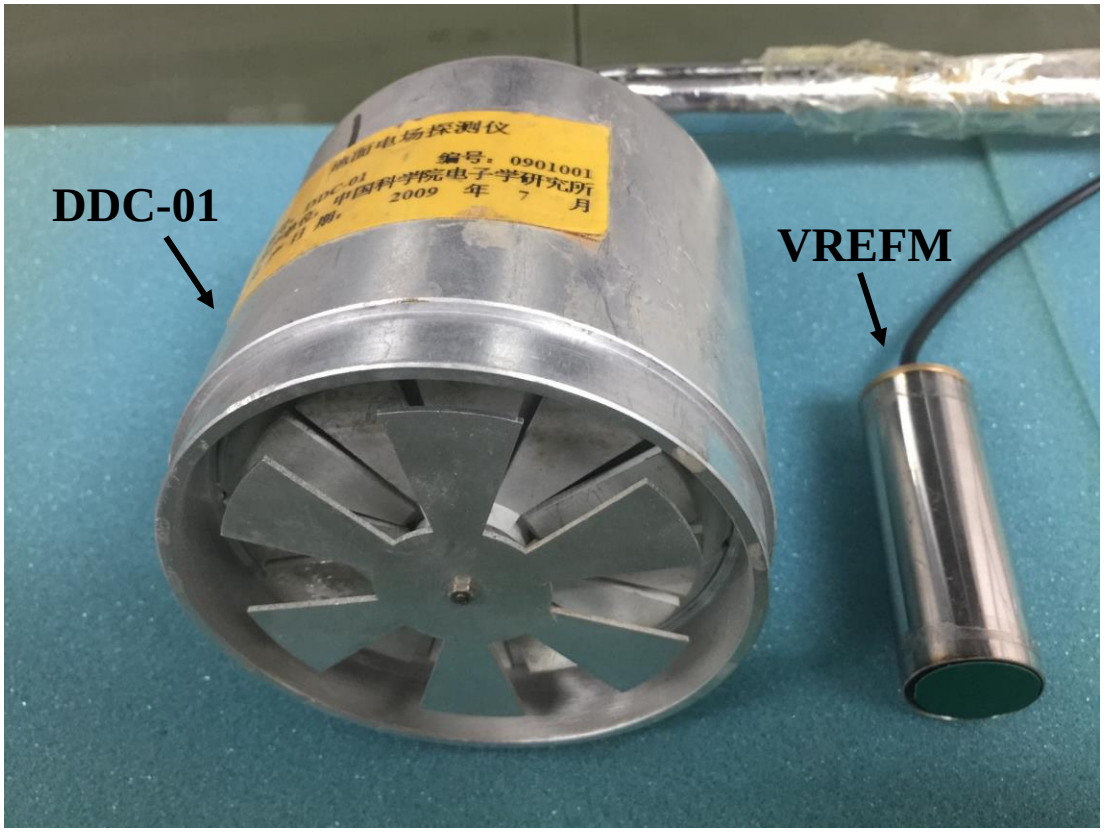

Fig. S8. Left: Higher accuracy atmospheric electric field mill (Model DDC-01) developed by Institute of Electrics, Chinese Academy of Sciences. Right: The VREFM sensors used in this study.

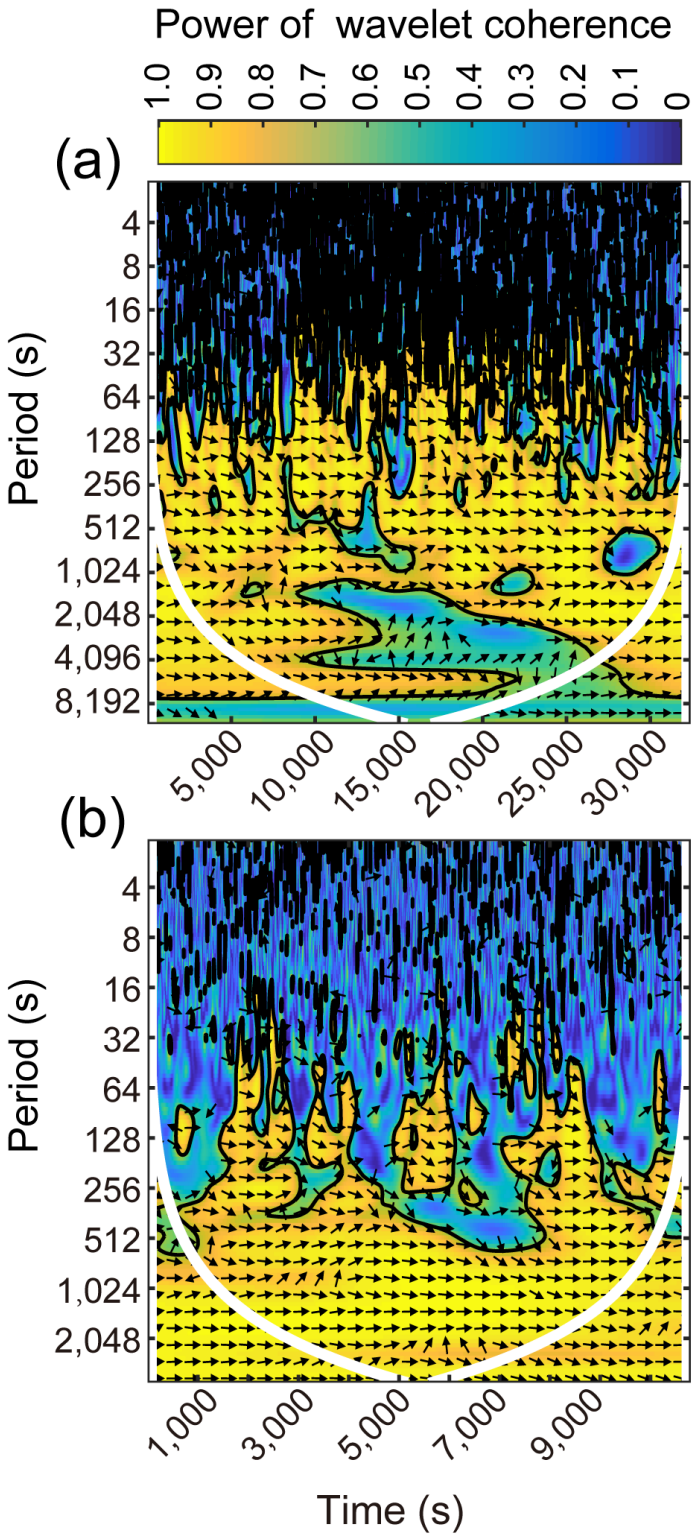

Fig. S9. The relative phase relationship between the space charge density and dust concentration. (a) and (b) correspond to No. 1-2 dust storms, respectively. Arrows pointing right represent in-phase; arrows pointing left represent anti-phase.

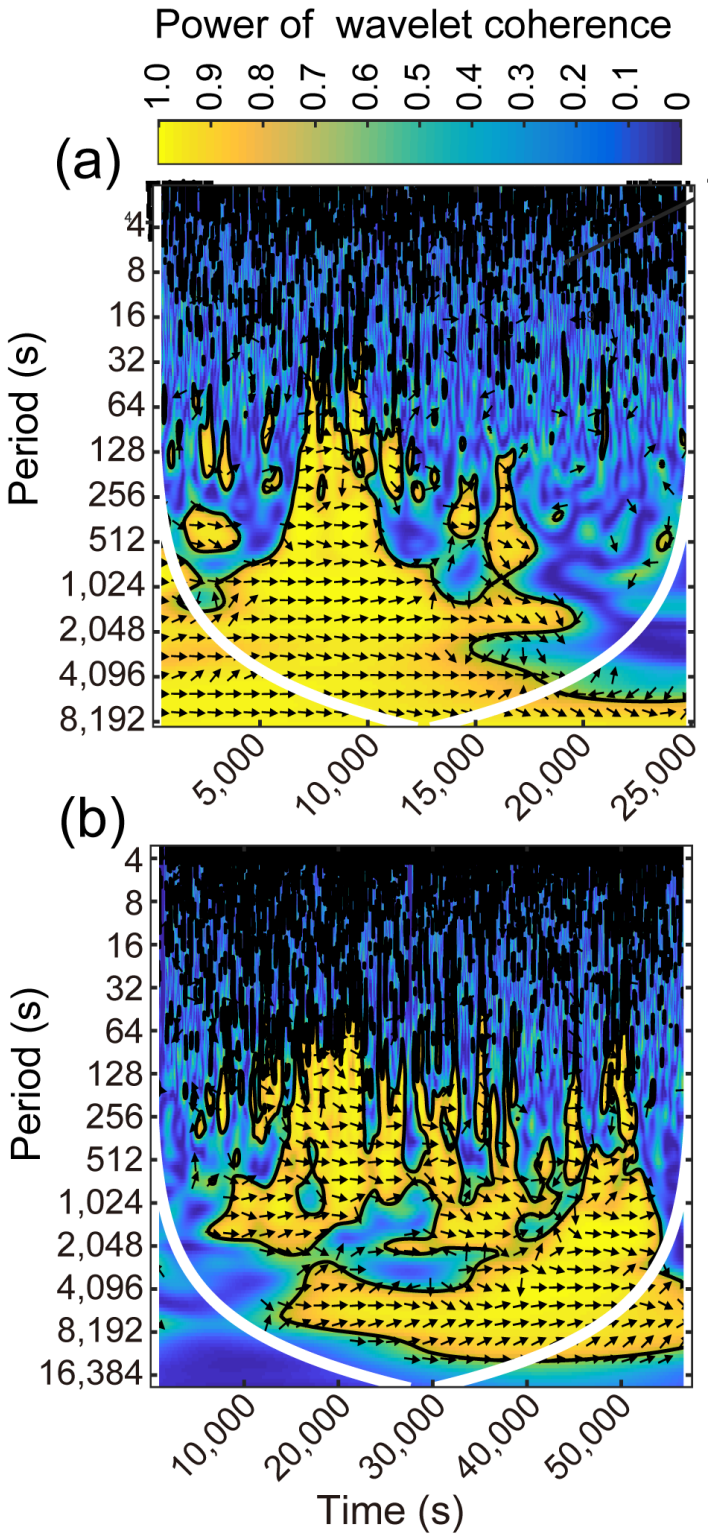

Fig. S10. The relative phase relationship between the space charge density and dust concentration. (a) and (b) correspond to No. 3-4 dust storms, respectively. Arrows pointing right represent in-phase; arrows pointing left represent anti-phase.

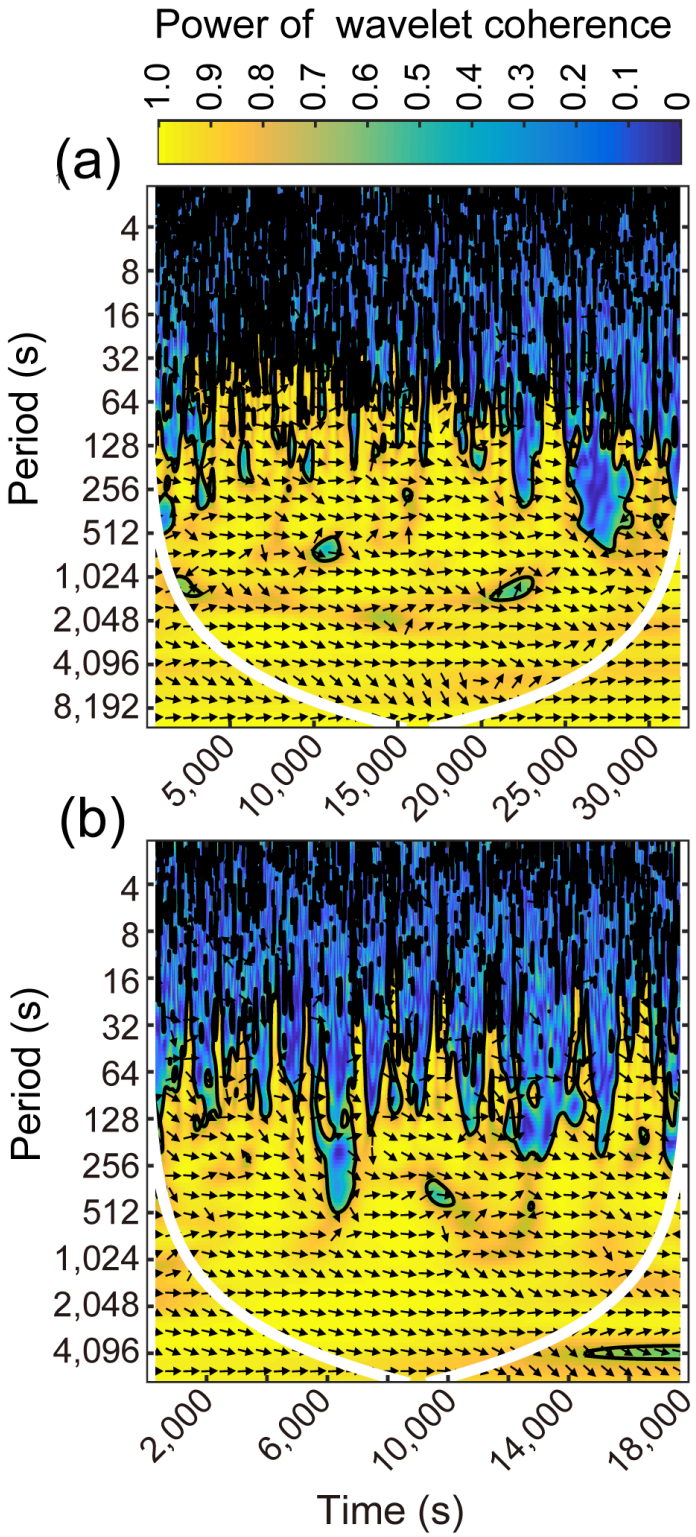

Fig. S11. The relative phase relationship between the space charge density and dust concentration. (a) and (b) correspond to No. 5-6 dust storms, respectively. Arrows pointing right represent in-phase; arrows pointing left represent anti-phase.

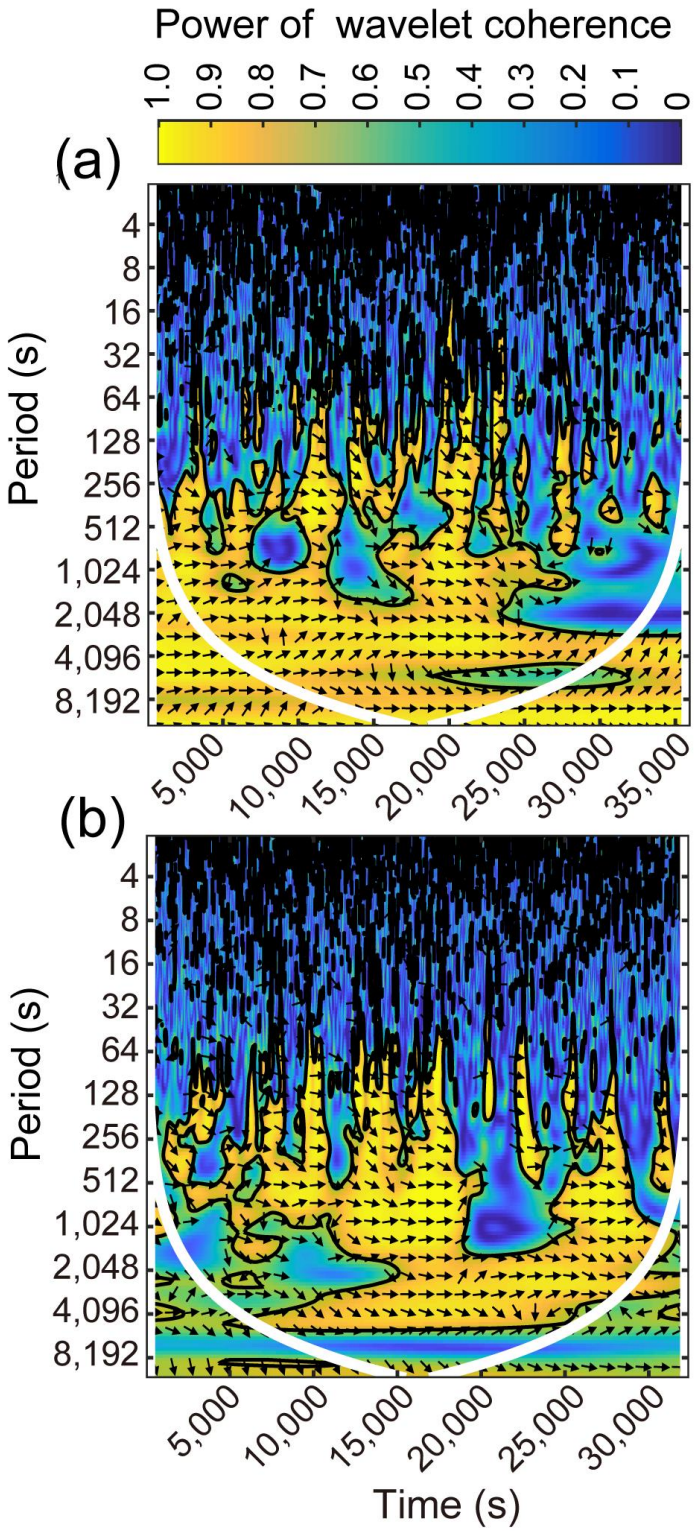

Fig. S12. The relative phase relationship between the space charge density and dust concentration. (a) and (b) correspond to No. 7-8 dust storms, respectively. Arrows pointing right represent in-phase; arrows pointing left represent anti-phase.

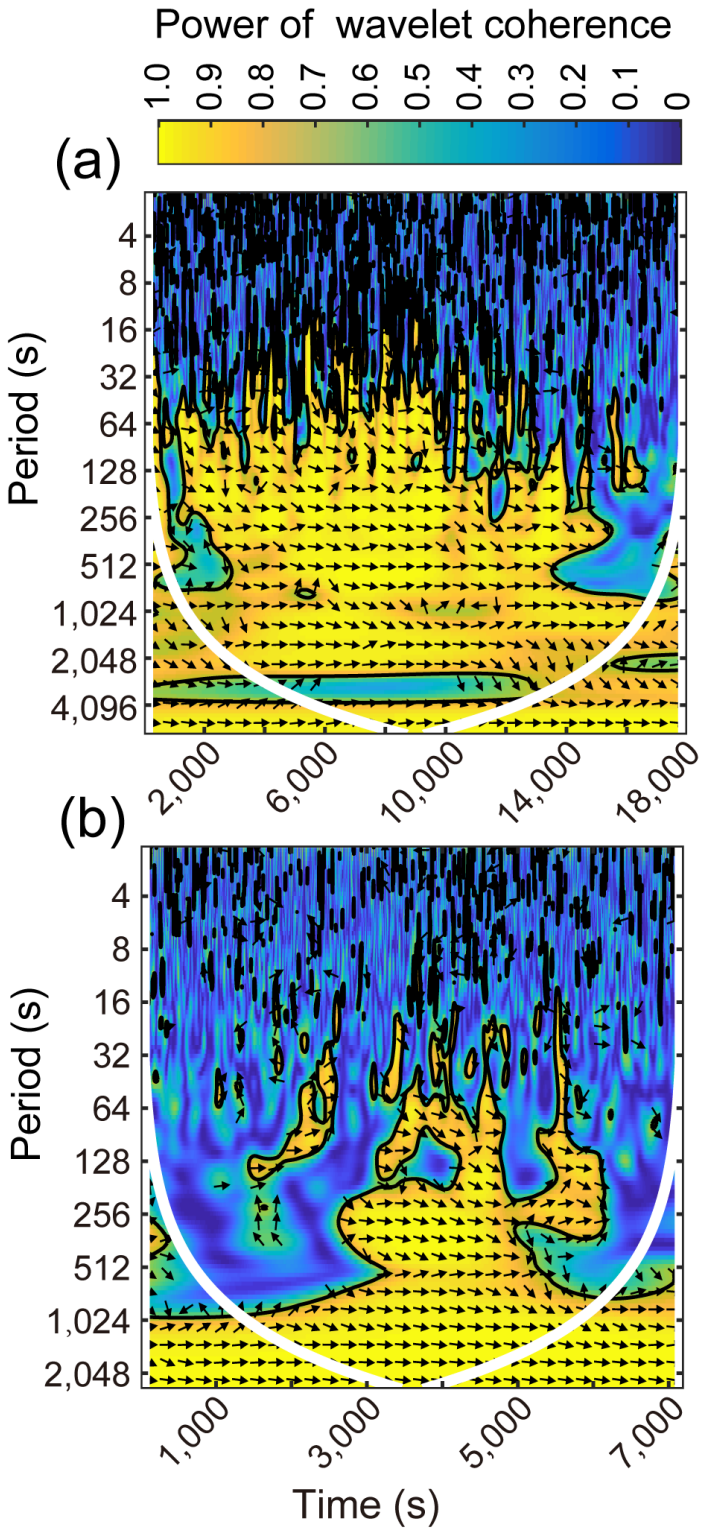

Fig. S13. The relative phase relationship between the space charge density and dust concentration. (a) and (b) correspond to No. 9-10 dust storms, respectively. Arrows pointing right represent in-phase; arrows pointing left represent anti-phase.